

Efficient tandem electroreduction of nitrate into ammonia through coupling Cu single atoms with adjacent Co_3O_4

Received: 5 October 2023

Accepted: 17 April 2024

Published online: 29 April 2024

Check for updates

Yan Liu^{1,7}, Jie Wei^{1,7}, Zhengwu Yang^{1,7}, Lirong Zheng², Jiankang Zhao¹, Zhimin Song¹, Yuhan Zhou¹, Jiajie Cheng³, Junyang Meng¹, Zhigang Geng¹✉ & Jie Zeng^{1,4,5,6}✉

The nitrate (NO_3^-) electroreduction into ammonia (NH_3) represents a promising approach for sustainable NH_3 synthesis. However, the variation of adsorption configurations renders great difficulties in the simultaneous optimization of binding energy for the intermediates. Though the extensively reported Cu-based electrocatalysts benefit NO_3^- adsorption, one of the key issues lies in the accumulation of nitrite (NO_2^-) due to its weak adsorption, resulting in the rapid deactivation of catalysts and sluggish kinetics of subsequent hydrogenation steps. Here we report a tandem electrocatalyst by combining Cu single atoms catalysts with adjacent Co_3O_4 nanosheets to boost the electroreduction of NO_3^- to NH_3 . The obtained tandem catalyst exhibits a yield rate for NH_3 of $114.0 \text{ mg}_{\text{NH}_3} \text{ h}^{-1} \text{ cm}^{-2}$, which exceeds the previous values for the reported Cu-based catalysts. Mechanism investigations unveil that the combination of Co_3O_4 regulates the adsorption configuration of NO_2^- and strengthens the binding with NO_2^- , thus accelerating the electroreduction of NO_3^- to NH_3 .

As one of the nitrogen-containing species, nitrate (NO_3^-) widely exists in industrial and agricultural wastewater with a high concentration, mainly caused by the emission of low-level nuclear waste and intensive usage of fertilizers^{1–3}. Excessive NO_3^- has significantly threatened ecological balance, inducing acid rain and photochemical smog⁴. Additionally, NO_3^- in human body is easily converted into toxic nitrite (NO_2^-), leading to serious health issues⁵. Among the methods for removing NO_3^- , electroreduction process using renewable electricity is regarded as an appealing technology under mild conditions^{6–9}. The controllable products including nontoxic nitrogen (N_2) and valuable ammonia (NH_3) could be obtained after NO_3^- electroreduction^{10–12}.

Since NH_3 is a fundamental chemical compound and a promising green hydrogen carrier, NO_3^- electroreduction into NH_3 instead of N_2 is more desirable. Taken together, it is highly imperative to achieve efficient electroreduction of NO_3^- into NH_3 from the perspective of environmental protection and sustainable NH_3 synthesis.

In view of the multiple nitrogen-containing intermediates (e.g. $^*\text{NO}_3$, $^*\text{NO}_2$, and $^*\text{NO}$) involved in the NO_3^- electroreduction, an optimal catalyst should satisfy the simultaneously optimized adsorption of intermediates. The moderate binding energy of intermediates serves as one of the key factors for efficient NO_3^- electroreduction into NH_3 ^{13,14}. Classically, given that the coordination of N atom in NO_3^- is

¹Hefei National Research Center for Physical Sciences at the Microscale, University of Science and Technology of China, Hefei 230026 Anhui, PR China.

²Institute of High Energy Physics, Chinese Academy of Sciences, 100049 Beijing, PR China. ³Department of Physics, University of Science and Technology of China, Hefei 230026 Anhui, PR China. ⁴CAS Key Laboratory of Strongly-Coupled Quantum Matter Physics, University of Science and Technology of China, Hefei 230026 Anhui, PR China. ⁵Key Laboratory of Surface and Interface Chemistry and Energy Catalysis of Anhui Higher Education Institutes, Department of Chemical Physics, University of Science and Technology of China, Hefei 230026 Anhui, PR China. ⁶School of Chemistry & Chemical Engineering, Anhui University of Technology, Ma'anshan 243002 Anhui, PR China. ⁷These authors contributed equally: Yan Liu, Jie Wei, Zhengwu Yang.

✉ e-mail: gengzg@ustc.edu.cn; zengj@ustc.edu.cn

saturated by three O atoms, *NO_3 tends to bond with active sites through O atoms. Whereas, *NO_2 is preferentially adsorbed on active sites through N and O atoms. As for *NO , N atom in *NO is inclined to connect with active sites. The variation of adsorption configurations renders great difficulties in the simultaneous optimization of binding energy for the intermediates. A typical instance is Cu-based electrocatalysts which have been reported extensively for NO_3^- electroreduction^{14–20}. Though Cu-based electrocatalysts benefit NO_3^- adsorption, one of the key issues lies in the accumulation of NO_2^- , resulting in the rapid deactivation of catalysts and sluggish kinetics of the subsequent hydrogenation steps for NH_3 production^{15,17}. However, it remains a grand challenge to design an efficient catalyst to satisfy the simultaneously optimized adsorption of intermediates with different configurations.

Herein, we report a tandem electrocatalyst by combining Cu single atoms anchored on N-doped carbon with adjacent Co_3O_4 nanosheets (denoted as Co_3O_4/Cu_1-N-C) to boost the electroreduction of NO_3^- to NH_3 . The obtained Co_3O_4/Cu_1-N-C catalyst exhibits a remarkable yield rate for NH_3 of $114.0 \text{ mg}_{NH_3} \text{ h}^{-1} \text{ cm}^{-2}$, which exceeds the previous values for all of the reported Cu-based catalysts. Mechanism investigations unveil that the combination of Co_3O_4

regulates the adsorption configuration of NO_2^- and strengthens the binding with NO_2^- , thus accelerating the electroreduction of NO_3^- to NH_3 .

Results

Catalyst synthesis and characterizations

Co_3O_4/Cu_1-N-C catalyst was synthesized by adding sodium borohydride to the mixture containing Cu single-atom catalysts and cobalt nitrate. Cu single atoms dispersed on N-doped carbon (denoted as Cu_1-N-C) were prepared via pyrolyzing Cu-doped ZIF-8 at 900°C under Ar atmosphere (Supplementary Figs. 1 and 2). Figure 1a shows the high-angle annular dark field scanning transmission electron microscopy (HAADF-STEM) image of Co_3O_4/Cu_1-N-C . As displayed in the high resolution TEM (HRTEM) image and the corresponding selected area electron diffraction pattern (SAED), Co_3O_4 nanosheets were successfully deposited on the surface of Cu_1-N-C (Supplementary Fig. 3). Figure 1b shows the aberration-corrected HAADF-STEM image of Co_3O_4/Cu_1-N-C . The lattice fringes with an interplanar spacing of 0.201 nm were ascribed to the (400) facet of Co_3O_4 . Besides, abundant Cu single atoms were observed around Co_3O_4 nanosheets. Based on energy-dispersive X-ray spectroscopy (EDS) elemental mapping, Co, Cu, and N

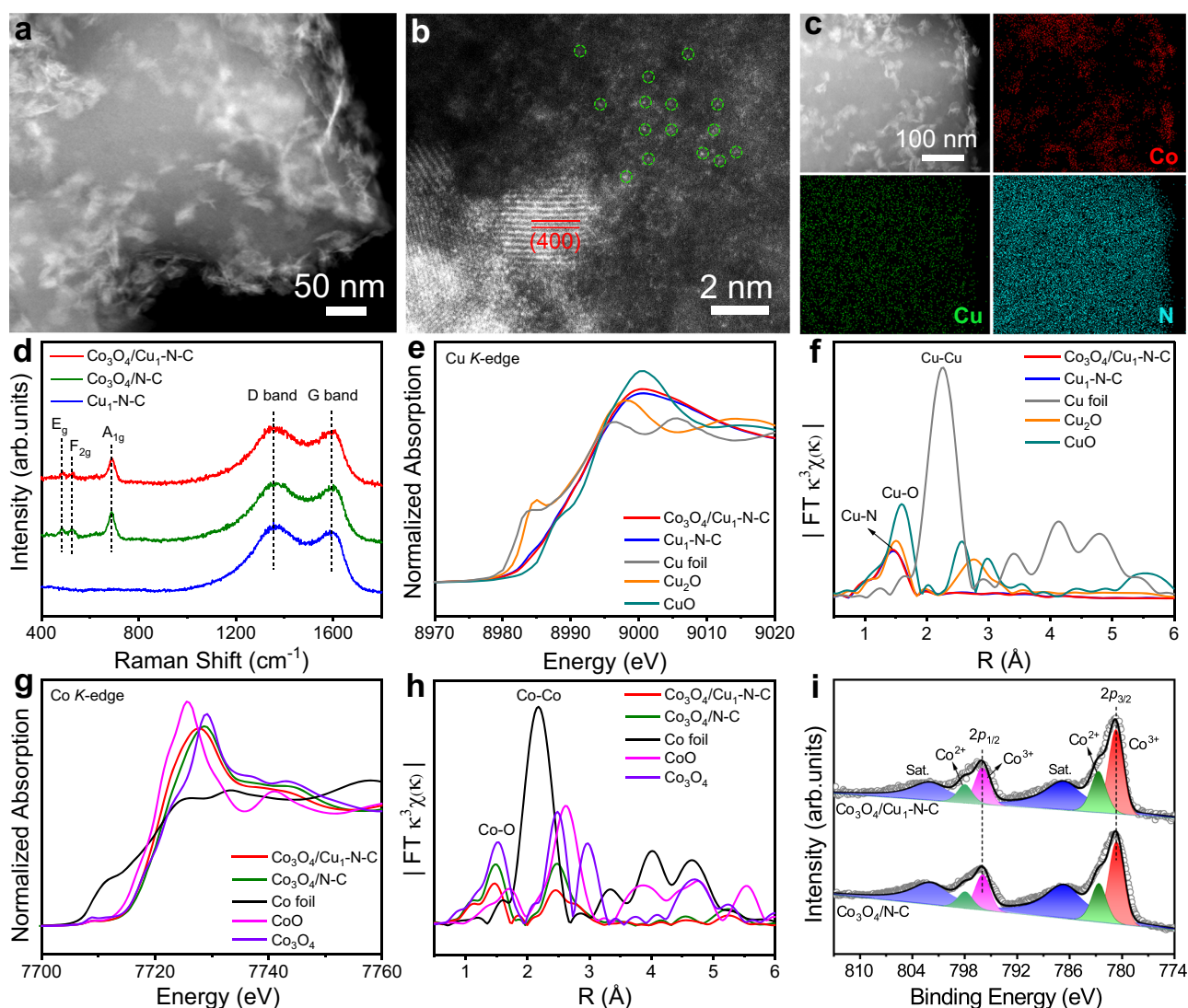


Fig. 1 | Structural characterizations. **a** HAADF-STEM image, **b** aberration-corrected HAADF-STEM image, and **c** EDS elemental mappings of Co_3O_4/Cu_1-N-C . **d** Raman spectra of Co_3O_4/Cu_1-N-C , Cu_1-N-C , and $Co_3O_4/N-C$. **e** Cu K-edge XANES

spectra and **f** EXAFS spectra for Co_3O_4/Cu_1-N-C , Cu_1-N-C , Cu foil, Cu_2O , and CuO. **g** Co K-edge XANES spectra and **h** EXAFS spectra for Co_3O_4/Cu_1-N-C , $Co_3O_4/N-C$, Co foil, CoO, and Co_3O_4 . **i** Co 2p XPS spectra for Co_3O_4/Cu_1-N-C and $Co_3O_4/N-C$.

elements were uniformly distributed throughout the whole structure (Fig. 1c). The uniform distribution of Cu sites and Co_3O_4 species constituted the adjacent catalytic centers. The metal content of Cu and Co in $\text{Co}_3\text{O}_4/\text{Cu}_1\text{-N-C}$ were determined to be 0.60 wt% and 4.70 wt%, respectively, by inductively coupled plasma-optical emission spectroscopy analysis (ICP-OES). For comparison, Co_3O_4 nanosheets dispersed on N-doped carbon (denoted as $\text{Co}_3\text{O}_4/\text{N-C}$) were prepared with a similar synthetic procedure of $\text{Co}_3\text{O}_4/\text{Cu}_1\text{-N-C}$ except for the addition of Cu precursor (Supplementary Fig. 4). Figure 1d shows the Raman spectra for $\text{Co}_3\text{O}_4/\text{Cu}_1\text{-N-C}$, $\text{Cu}_1\text{-N-C}$, and $\text{Co}_3\text{O}_4/\text{N-C}$. All of the Raman spectra displayed two peaks located at 1356 and 1591 cm^{-1} , assigned to the D band and G band of graphite carbon, respectively²¹. The similar intensity ratios of D band to G band ($I_{\text{D}}/I_{\text{G}}$) for the three samples indicated that the carbon support possessed similar degree of structural disorder (Supplementary Fig. 5). Compared with $\text{Cu}_1\text{-N-C}$, three distinguishable peaks located at 482, 527, and 689 cm^{-1} were observed for both $\text{Co}_3\text{O}_4/\text{Cu}_1\text{-N-C}$ and $\text{Co}_3\text{O}_4/\text{N-C}$, corresponding to E_{g} , $F_{2\text{g}}$, and $A_{1\text{g}}$ vibration modes of Co_3O_4 crystals, respectively²². The structure of graphite carbon supports was further confirmed by X-ray diffraction patterns (Supplementary Fig. 6). Figure 1e shows the Cu *K*-edge X-ray absorption near edge structure (XANES) spectra of $\text{Co}_3\text{O}_4/\text{Cu}_1\text{-N-C}$ and $\text{Cu}_1\text{-N-C}$. Obviously, the energy absorption edge profiles for both $\text{Co}_3\text{O}_4/\text{Cu}_1\text{-N-C}$ and $\text{Cu}_1\text{-N-C}$ were located between those of CuO and Cu_2O , elucidating that the valence state of Cu species in the two catalysts were between +1 to +2. As shown in Fig. 1f, a dominant peak at 1.93 Å was observed in the extended X-ray absorption fine structure (EXAFS) spectra of Cu *K*-edge for $\text{Co}_3\text{O}_4/\text{Cu}_1\text{-N-C}$ and $\text{Cu}_1\text{-N-C}$, which were attributed to the Cu-N bond. The absence of Cu-Cu bond in the two catalysts further confirmed the atomic dispersion of Cu species. Besides, the EXAFS fitting results indicate that the coordination numbers of Cu-N shell in both $\text{Co}_3\text{O}_4/\text{Cu}_1\text{-N-C}$ and $\text{Cu}_1\text{-N-C}$ were approximately 4.0 (Supplementary Fig. 7 and Table 1). After the deposition of Co_3O_4 nanosheets, the coordination structure of Cu single atoms (CuN_4) in $\text{Co}_3\text{O}_4/\text{Cu}_1\text{-N-C}$ was unchanged. Besides, the wavelet transformed EXAFS (WT-EXAFS) spectra of $\text{Co}_3\text{O}_4/\text{Cu}_1\text{-N-C}$ and $\text{Cu}_1\text{-N-C}$ also confirmed the Cu-N bonding in the two catalysts (Supplementary Fig. 8). For the Co *K*-edge XANES spectra, the edge energy for both $\text{Co}_3\text{O}_4/\text{Cu}_1\text{-N-C}$ and $\text{Co}_3\text{O}_4/\text{N-C}$ were similar to that for Co_3O_4 reference (Fig. 1g). Figure 1h shows that the Co-O coordination in $\text{Co}_3\text{O}_4/\text{Cu}_1\text{-N-C}$ and $\text{Co}_3\text{O}_4/\text{N-C}$ were approximate to that in Co_3O_4 , certifying the similar coordination structure of Co_3O_4 species in the two catalysts (Supplementary Fig. 9 and Table 2). Figure 1i shows the Co 2*p* X-ray photoelectron spectroscopy (XPS) spectra. Specifically, the peaks at 798.0, 782.7, 796.1, and 780.8 eV in $\text{Co}_3\text{O}_4/\text{Cu}_1\text{-N-C}$ and $\text{Co}_3\text{O}_4/\text{N-C}$ corresponded to $\text{Co}^{2+} 2p_{1/2}$, $\text{Co}^{2+} 2p_{3/2}$, $\text{Co}^{3+} 2p_{1/2}$, and $\text{Co}^{3+} 2p_{3/2}$, respectively²³. The indiscernible shift of Co 2*p* peaks demonstrated that $\text{Cu}_1\text{-N-C}$ as the support did not significantly affect the valence state of Co.

Catalytic performance toward NO_3^- electroreduction

The catalytic performance of the catalysts was investigated in a three-electrode H-type cell toward NO_3^- electroreduction (Supplementary Fig. 10). The concentration of NH_3 product was quantified by the indophenol blue method (Supplementary Fig. 11). To preliminarily explore the process of tandem catalysis, we conducted the linear sweep voltammetry (LSV) curves of $\text{Co}_3\text{O}_4/\text{Cu}_1\text{-N-C}$, $\text{Cu}_1\text{-N-C}$, and $\text{Co}_3\text{O}_4/\text{N-C}$ with 1 M $\text{NO}_3^-/\text{NO}_2^-$, respectively. As shown in Fig. 2a, the current density of $\text{Cu}_1\text{-N-C}$ in the presence of NO_3^- was higher than that of $\text{Co}_3\text{O}_4/\text{N-C}$, suggesting that $\text{Cu}_1\text{-N-C}$ possessed higher activity toward NO_3^- electroreduction. Whereas, $\text{Co}_3\text{O}_4/\text{N-C}$ exhibited a larger current density relative to $\text{Cu}_1\text{-N-C}$ in NO_2^- (Fig. 2b). The superior activity of Co_3O_4 species toward NO_2^- electroreduction was further demonstrated by the higher Faradaic efficiency (FE) and yield rate for NH_3 of $\text{Co}_3\text{O}_4/\text{N-C}$ in NO_2^- electroreduction relative to $\text{Cu}_1\text{-N-C}$ (Supplementary Fig. 12). Considering that NO_2^- is one of the vital

intermediates, the combination of $\text{Cu}_1\text{-N-C}$ and Co_3O_4 would couple the separate functions of Cu sites and Co_3O_4 species for the sequential reduction of NO_3^- and NO_2^- . As expected, $\text{Co}_3\text{O}_4/\text{Cu}_1\text{-N-C}$ displayed the highest current density among the three catalysts in the electrolyte of NO_3^- . Besides, the tremendous discrepancy of the LSV curves of $\text{Co}_3\text{O}_4/\text{Cu}_1\text{-N-C}$ in 1 M KOH with/without NO_3^- also implied the superior activity of $\text{Co}_3\text{O}_4/\text{Cu}_1\text{-N-C}$ toward NO_3^- electroreduction (Supplementary Fig. 13).

Figure 2c provides the partial current density for NH_3 (j_{NH_3}) of $\text{Co}_3\text{O}_4/\text{Cu}_1\text{-N-C}$, $\text{Cu}_1\text{-N-C}$, and $\text{Co}_3\text{O}_4/\text{N-C}$ at various applied potentials toward NO_3^- electroreduction. The j_{NH_3} of $\text{Co}_3\text{O}_4/\text{Cu}_1\text{-N-C}$ exceeded those of $\text{Cu}_1\text{-N-C}$ and $\text{Co}_3\text{O}_4/\text{N-C}$. Especially, at -1.0 V *vs* reversible hydrogen electrode (RHE), the j_{NH_3} of $\text{Co}_3\text{O}_4/\text{Cu}_1\text{-N-C}$ reached -1437.5 mA cm^{-2} , which was 2.2 times and 3.6 times as high as that of $\text{Cu}_1\text{-N-C}$ and $\text{Co}_3\text{O}_4/\text{N-C}$, respectively. Moreover, the normalized j_{NH_3} based on double-layer capacitance (C_{dl}) for $\text{Co}_3\text{O}_4/\text{Cu}_1\text{-N-C}$ was the largest among the three catalysts, indicating the highest intrinsic activity for $\text{Co}_3\text{O}_4/\text{Cu}_1\text{-N-C}$ toward NO_3^- electroreduction (Fig. 2d and Supplementary Fig. 14). In addition, the FE for NH_3 of $\text{Co}_3\text{O}_4/\text{Cu}_1\text{-N-C}$ was higher with respect to the other two counterparts at all applied potentials (Fig. 2e). Especially, $\text{Co}_3\text{O}_4/\text{Cu}_1\text{-N-C}$ achieved the maximum FE for NH_3 of 97.7% at -0.8 V *vs* RHE. Furthermore, at -1.0 V *vs* RHE, the yield rate of NH_3 for $\text{Co}_3\text{O}_4/\text{Cu}_1\text{-N-C}$ reached up to 114.0 $\text{mg}_{\text{NH}_3} \text{h}^{-1} \text{cm}^{-2}$, which exceeded all of the reported value for Cu-based catalysts^{14,16,18,19,24–30} (Fig. 2f and Supplementary Table 3). The yield rate of NH_4^+ in the electrolyte after the electroreduction process was also determined by ^1H nuclear magnetic resonance (NMR) analysis, which was approximated to the results detected via the indophenol blue method (Supplementary Fig. 15 and Table 4). Other liquid and gaseous products including NO_2^- , NH_2OH , NO , NO_2 , N_2O , H_2 , and N_2 for $\text{Co}_3\text{O}_4/\text{Cu}_1\text{-N-C}$ were also measured (Supplementary Figs. 16–18). NH_3 were the only main product after $\text{NO}_3^-/\text{NO}_2^-$ electroreduction (Supplementary Table 5). Besides, the FE for NH_3 of $\text{Co}_3\text{O}_4/\text{Cu}_1\text{-N-C}$ with NO_3^- concentrations ranging from 10 mM to 500 mM all exceeded 91.2%, indicating a wide tolerance range for the concentration of NO_3^- (Supplementary Fig. 19). The durability of $\text{Co}_3\text{O}_4/\text{Cu}_1\text{-N-C}$ was examined by 20 rounds of successive reactions. The negligible decay of the yield rate demonstrated the satisfactory durability of $\text{Co}_3\text{O}_4/\text{Cu}_1\text{-N-C}$ (Fig. 2g). The Raman and XAFS measurements for $\text{Co}_3\text{O}_4/\text{Cu}_1\text{-N-C}$ after the electrolysis indicated that the Co_3O_4 species and Cu-N bonding were preserved (Supplementary Figs. 20 and 21). The stability of Cu single atoms in $\text{Co}_3\text{O}_4/\text{Cu}_1\text{-N-C}$ during the electrolysis was further explored by in situ EXAFS measurements, indicating that Cu atoms remained the atomically dispersed state in $\text{Co}_3\text{O}_4/\text{Cu}_1\text{-N-C}$ during the NO_3^- electroreduction (Supplementary Figs. 22 and 23).

To further clarify the synergy effect of Co_3O_4 on the conversion of NO_2^- , we conducted a series of control experiments. The catalytic performance of other metal oxides (such as FeO_x , CuO_x , and NiO_x) dispersed on N-doped carbon toward NO_2^- electroreduction were all lower than that over $\text{Co}_3\text{O}_4/\text{N-C}$, suggesting the inferior ability of these metal oxide to facilitate NO_2^- reduction (Supplementary Figs. 24 and 25). In addition, the loading amount of Co_3O_4 on $\text{Cu}_1\text{-N-C}$ was vital to the efficient conversion of the accumulated NO_2^- (Supplementary Fig. 26). Besides, the simply physical mixing of $\text{Cu}_1\text{-N-C}$ and $\text{Co}_3\text{O}_4/\text{N-C}$ could not sufficiently assure the spatial couple of the adjacent sites, thereby limiting the effective hydrogenation of NO_2^- into NH_3 during NO_3^- electroreduction (Supplementary Fig. 27). We also exclude the possible ammonia contamination from the self-electrolysis of $\text{Co}_3\text{O}_4/\text{Cu}_1\text{-N-C}$, electrolyte, and carbon paper, respectively (Supplementary Fig. 28). Besides, the catalytic activity of N-doped carbon was much lower compared with that of $\text{Co}_3\text{O}_4/\text{Cu}_1\text{-N-C}$ (Supplementary Fig. 29). The possible interference of Co single atoms on $\text{Cu}_1\text{-N-C}$ support could be considered insignificant to the catalytic performance of $\text{Co}_3\text{O}_4/\text{Cu}_1\text{-N-C}$ (Supplementary Figs. 30–33). The electroreduction of NO_3^- was also affected by the diffusion of

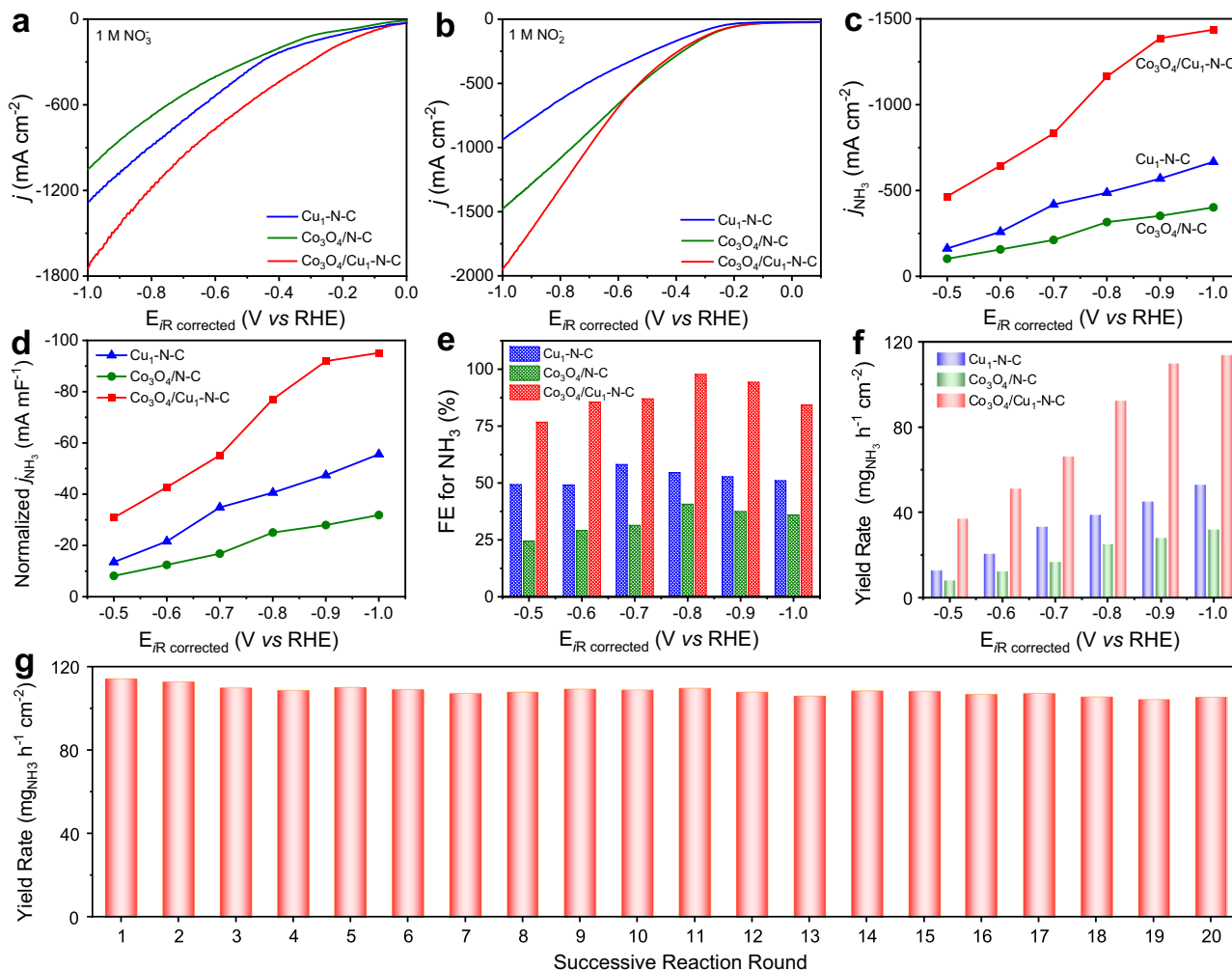


Fig. 2 | Catalytic performance. LSV curves of Cu₁-N-C, Co₃O₄/N-C, and Co₃O₄/Cu₁-N-C with (a) 1 M NO₃⁻ and (b) 1 M NO₂⁻. c j_{NH_3} , d normalized j_{NH_3} based on C_{dl} , e FE for NH₃, and f yield rate for NH₃ of Cu₁-N-C, Co₃O₄/N-C, and Co₃O₄/Cu₁-N-C at different applied potentials with 1 M NO₃⁻. g Yield rate for NH₃ of Co₃O₄/Cu₁-N-C at

-1.0 V *vs* RHE under 20 rounds of successive reactions. The solution resistance was determined to be 4.4 ± 0.2 ohm in the electrolytes by potentiostatic electrochemical impedance spectroscopy.

reactants (Supplementary Fig. 34). Moreover, ¹⁵NO₃⁻ isotopic labeling measurements for Co₃O₄/Cu₁-N-C was conducted with ¹H NMR analysis. Only typical doublet peaks attributed to ¹⁵NH₄⁺ were collected with ¹⁵NO₃⁻ as the N source whereas the triplet peaks of ¹⁴NH₄⁺ were detected with ¹⁴NO₃⁻ as the N source (Supplementary Fig. 35). These results indicated that the NH₃ detected in the electrolyte originated from the electroreduction of NO₃⁻.

Mechanistic study on NO₃⁻ electroreduction

To gain more insight into the catalytic process of NO₃⁻ electroreduction over Co₃O₄/Cu₁-N-C, we conducted in situ electrochemical Fourier transform infrared spectroscopy (FTIR) and Raman spectroscopy to monitor the reaction process (Supplementary Figs. 36 and 37). Figure 3a displays the in situ FTIR spectra of Co₃O₄/Cu₁-N-C at applied potentials from OCP to -1.0 V *vs* RHE. The negative peaks at 1382 cm⁻¹ were ascribed to the consumption of NO₃⁻ species³. In addition, the emergence of positive peaks located at 1456 cm⁻¹ confirmed that NH₄⁺ was generated during the NO₃⁻ electroreduction³¹. Besides, two peaks at 1541 and 1508 cm⁻¹ were detected, which were assigned to the vibration band of *NO and *NOH, respectively (Supplementary Fig. 38). Figure 3b shows the in situ Raman spectra of Co₃O₄/Cu₁-N-C at all applied potentials. The peaks corresponding to E_g, F_{2g}, and A_{1g} vibration modes of Co₃O₄ remained unchanged, suggesting that the Co₃O₄

species was stable during NO₃⁻ electroreduction. During the NO₃⁻ electroreduction, only the peak at 1049 cm⁻¹ was observed for Co₃O₄/Cu₁-N-C at all applied potentials, assigned to the symmetric stretching vibration of NO₃⁻ (Fig. 3c). In the case of Cu₁-N-C, apart from the signal of NO₃⁻, a new peak at 810 cm⁻¹ ascribed to the bending vibration of NO₂⁻ gradually appeared as the applied potential increased, indicating the accumulation of NO₂⁻ for Cu₁-N-C during NO₃⁻ electroreduction (Fig. 3d). To further probe the variation of local concentration for NO₂⁻ near the surface of the catalysts, we designed a Raman cell that allows Raman laser to detect from the surface of catalysts to the electrolyte bulk. The Raman laser was designed to be incident from the back of catalysts to diminish the interference from the strong absorbance of NO₃⁻ in the electrolyte. As illustrated in Fig. 3e, the electrocatalysts were deposited on fluorine tin oxide-coated glass (FTO) as the working electrode (WE). The distance from the laser beam to electrode surface is controlled by the mechanical sample stage. Figure 3f, g display the in situ Raman spectra of Co₃O₄/Cu₁-N-C and Cu₁-N-C at -0.8 V *vs* RHE when the laser beam was positioned 0 to 200 μm away from the surface of catalysts, respectively. With the increment of the distance between the focal plane of laser and the surface of catalysts, the signal intensity of graphite carbon for the catalysts gradually decreased. A noticeable peak at 810 cm⁻¹ assigned to NO₂⁻ arose near the surface of Cu₁-N-C. Whereas, the signal of NO₂⁻ for Co₃O₄/Cu₁-N-C was negligible,

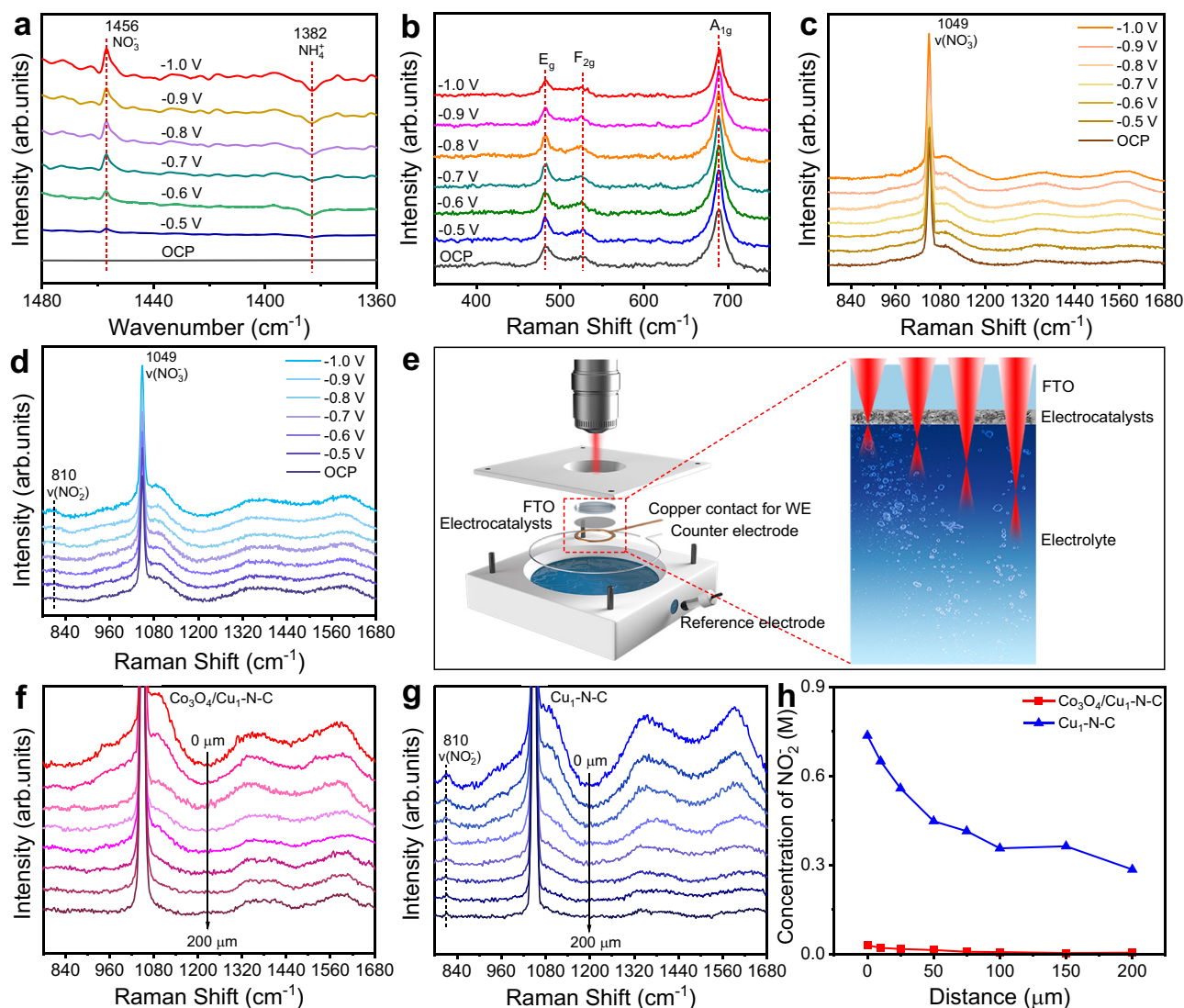


Fig. 3 | In situ characterizations. **a** In situ FTIR spectra for $\text{Co}_3\text{O}_4/\text{Cu}_1\text{-N-C}$ from OCP to -1.0 V vs RHE in 1 M NO_3^- . **b** In situ Raman spectra for $\text{Co}_3\text{O}_4/\text{Cu}_1\text{-N-C}$ from OCP to -1.0 V vs RHE in 1 M NO_3^- . In situ Raman spectra for (c) $\text{Co}_3\text{O}_4/\text{Cu}_1\text{-N-C}$ and (d) $\text{Cu}_1\text{-N-C}$ from OCP to -1.0 V vs RHE in 1 M NO_3^- . **e** Scheme of the designed Raman cell for detecting from the surface of catalysts to the electrolyte bulk. In situ Raman

spectra for (f) $\text{Co}_3\text{O}_4/\text{Cu}_1\text{-N-C}$ and (g) $\text{Cu}_1\text{-N-C}$ at -0.8 V vs RHE in 1 M NO_3^- with different distances ranging from 0 to $200\ \mu\text{m}$. **h** The calculated concentration of NO_2^- for $\text{Co}_3\text{O}_4/\text{Cu}_1\text{-N-C}$ and $\text{Cu}_1\text{-N-C}$ with different distances ranging from 0 to $200\ \mu\text{m}$.

which was independent of the distance. Furthermore, we determined the local concentration of NO_2^- near the surface of catalysts based on the integrated areas of NO_2^- and NO_3^- , taking the ratio of integrated areas for 1 M NO_2^- and 1 M NO_3^- solutions as a correction factor (Supplementary Fig. 39). As the laser beam was set further far away from the surface of catalysts into the electrolyte, the concentration of NO_2^- for $\text{Cu}_1\text{-N-C}$ gradually decreased from 0.74 to 0.29 M (Fig. 3h). This trend indicates that the NO_2^- generated at $\text{Cu}_1\text{-N-C}/\text{electrolyte}$ interface diffused into the electrolyte due to the sluggish reduction of NO_2^- . Clearly, the concentration of NO_2^- for $\text{Co}_3\text{O}_4/\text{Cu}_1\text{-N-C}$ was much lower relative to $\text{Cu}_1\text{-N-C}$, manifesting the facilitated reduction of NO_2^- with the favor of Co_3O_4 .

To further understand the synergetic role of $\text{Cu}_1\text{-N-C}$ and Co_3O_4 in the catalytic process, we calculated the rate constants for NO_3^- electroreduction (k_1) and NO_2^- electroreduction (k_2), respectively (Fig. 4a). The concentration of residual NO_3^- after the electroreduction process was quantified by UV-Vis spectrophotometry (Supplementary Fig. 40). Compared with $\text{Co}_3\text{O}_4/\text{N-C}$, the larger k_1 value of $\text{Cu}_1\text{-N-C}$ suggests that $\text{Cu}_1\text{-N-C}$ was more favorable for the conversion of NO_3^- to NO_2^- , but the

smaller k_2 value shows the slower kinetics for NO_2^- reduction. Accordingly, excessive NO_2^- would be desorbed into the electrolyte for $\text{Cu}_1\text{-N-C}$. Notably, the highest k_1 and k_2 of $\text{Co}_3\text{O}_4/\text{Cu}_1\text{-N-C}$ manifested the simultaneous acceleration of the conversion of NO_3^- to NO_2^- and NO_2^- to NH_3 . Besides, the tafel slopes of $\text{Co}_3\text{O}_4/\text{Cu}_1\text{-N-C}$, $\text{Co}_3\text{O}_4/\text{N-C}$, and $\text{Cu}_1\text{-N-C}$ in 1 M NO_3^- and 1 M NO_2^- imply that the combination of Co_3O_4 with $\text{Cu}_1\text{-N-C}$ facilitate the kinetics of NO_3^- and NO_2^- reduction during the catalytic process (Supplementary Fig. 41). Figure 4b shows the adsorption capacities (q_e) of $\text{Co}_3\text{O}_4/\text{Cu}_1\text{-N-C}$, $\text{Cu}_1\text{-N-C}$, and $\text{Co}_3\text{O}_4/\text{N-C}$ for NO_3^- and NO_2^- , respectively. It is obvious that $\text{Co}_3\text{O}_4/\text{Cu}_1\text{-N-C}$ exhibited the largest q_e for both NO_3^- and NO_2^- among the three catalysts. As a consequence, combining $\text{Cu}_1\text{-N-C}$ with Co_3O_4 was conducive to the conversion of both NO_3^- and NO_2^- .

The density functional theory (DFT) calculations were conducted to further interpret the reaction mechanism of NO_3^- electroreduction over $\text{Co}_3\text{O}_4/\text{Cu}_1\text{-N-C}$ catalysts. Based on the results of structural analysis, we adopted CuN_4 and Co_3O_4 (100) slabs as the models to calculate the Gibbs free energies (G) for each step involved in NO_3^- electroreduction, respectively (Supplementary Fig. 42). After the

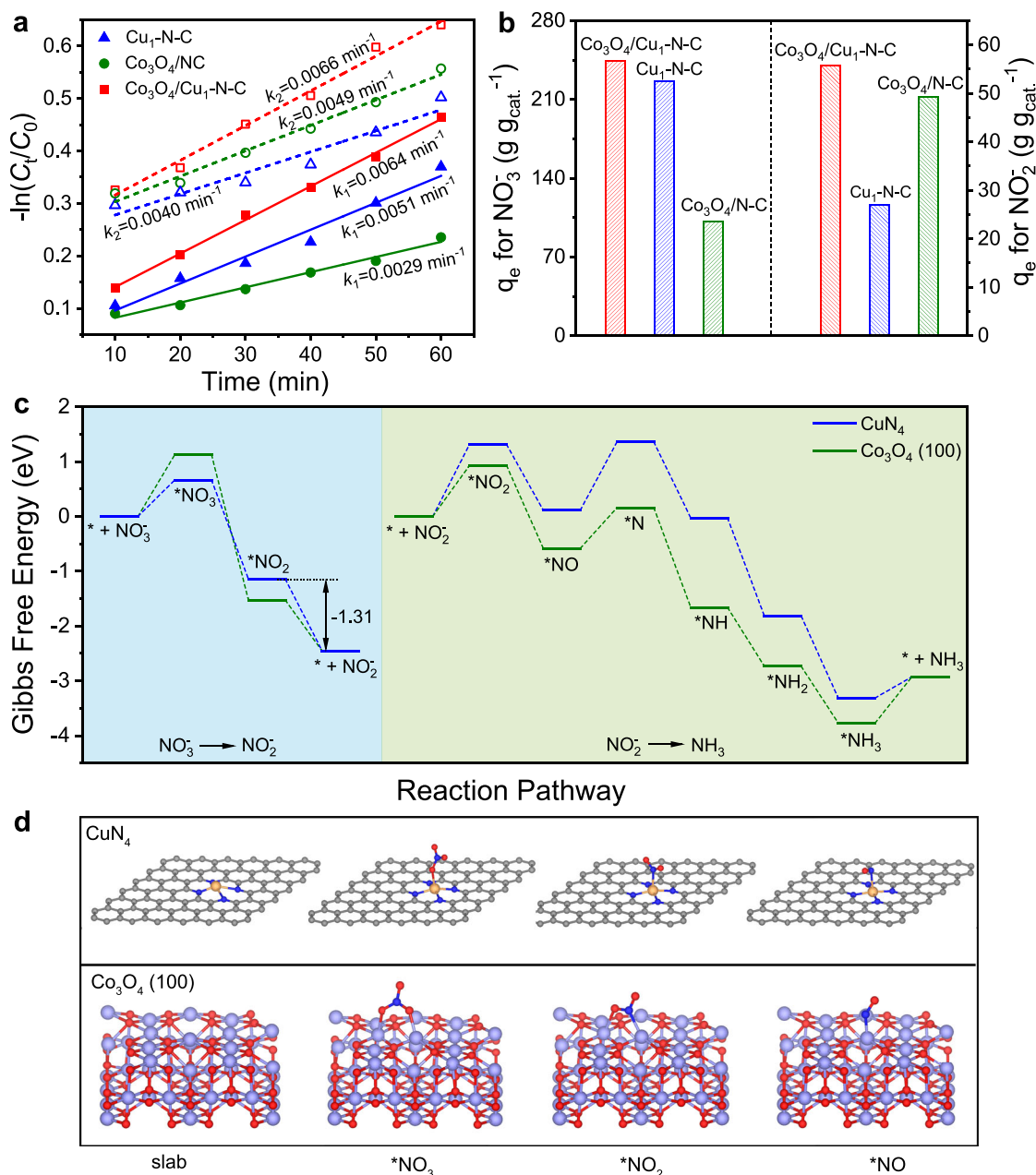


Fig. 4 | Mechanistic study on NO_3^- electroreduction. **a** Linearized pseudo first-order kinetic profiles of $\text{Co}_3\text{O}_4/\text{Cu}_1\text{-N-C}$, $\text{Cu}_1\text{-N-C}$, and $\text{Co}_3\text{O}_4/\text{N-C}$ in 1 M $\text{NO}_3^-/\text{NO}_2^-$, respectively. **b** Adsorption capacities of $\text{Co}_3\text{O}_4/\text{Cu}_1\text{-N-C}$, $\text{Cu}_1\text{-N-C}$, and $\text{Co}_3\text{O}_4/\text{N-C}$ for $\text{NO}_3^-/\text{NO}_2^-$. **c** Free energy diagram of NO_3^- electroreduction over CuN_4 and

Co_3O_4 (100) slabs. * represents an adsorption site. **d** Structure models of key intermediates on CuN_4 and Co_3O_4 (100) slabs. The gray, blue, red, yellow, and purple spheres represent C, N, O, Cu, and Co atoms, respectively.

structure optimization, $^*\text{NO}_3$ would be adsorbed on CuN_4 with O atom. As presented in Fig. 4c, the Gibbs free-energy changes (ΔG) for NO_3^- adsorption over CuN_4 is much lower than that over Co_3O_4 (100), indicating the stronger binding of NO_3^- over CuN_4 . Nevertheless, the ΔG of $^*\text{NO}_2$ desorption over CuN_4 is -1.31 eV , which could be more thermodynamically favorable than the reduction of $^*\text{NO}_2$ to $^*\text{NO}$ (-1.20 eV). In this regard, the desorption of $^*\text{NO}_2$ would give rise to the accumulation of NO_2^- over CuN_4 , which was consistent with the high yield for NO_2^- over $\text{Cu}_1\text{-N-C}$ in NO_3^- electroreduction (Supplementary Fig. 17). As for the conversion of NO_2^- , $^*\text{NO}_2$ would be adsorbed on CuN_4 through N atom whereas $^*\text{NO}_2$ could be connected with Co_3O_4 (100) through N and O atoms after the structure optimization, leading to the lower ΔG for NO_2^- adsorption over Co_3O_4 (100) (Fig. 4d). In addition, the relative high ΔG for $^*\text{H}$ adsorption over CuN_4 and Co_3O_4

revealed the weak adsorption of $^*\text{H}$, indicating that the occurrence of competitive H_2 evolution could be depressed (Supplementary Figs. 43 and 44). As a result, Co_3O_4 would regulate the adsorption configuration of NO_2^- and possess an easier binding with NO_2^- , facilitating the reduction of NO_2^- to NH_3 .

Discussion

In summary, we developed a highly efficient catalyst by coupling the separate functions of $\text{Cu}_1\text{-N-C}$ and Co_3O_4 for the sequential reduction of NO_3^- to NO_2^- and NO_2^- to NH_3 . The obtained $\text{Co}_3\text{O}_4/\text{Cu}_1\text{-N-C}$ catalyst exhibited a superior yield rate for NH_3 of $114.0 \text{ mg}_{\text{NH}_3} \text{ h}^{-1} \text{ cm}^{-2}$, which exceeded all of the reported values for Cu-based catalysts. The mechanism investigations unveiled that the combination of Co_3O_4 regulated the adsorption configuration of NO_2^- and strengthened the

binding with NO_2^- , thus accelerating the electroreduction of NO_3^- to NH_3 . This work offers a novel guideline for the construction of highly efficient tandem catalysts toward NO_3^- electroreduction.

Methods

Chemicals and materials

Zinc nitrate hexahydrate ($\text{Zn}(\text{NO}_3)_2 \cdot 6\text{H}_2\text{O}$, 99.0%), 2-methyl imidazole (2-MeIm, 99.0%), copper(II) acetate monohydrate ($\text{Cu}(\text{COOCH}_3)_2 \cdot \text{H}_2\text{O}$, 99.0%), cobalt nitrate hexahydrate ($\text{Co}(\text{NO}_3)_2 \cdot 6\text{H}_2\text{O}$, 99.0%), iron nitrate nonahydrate ($\text{Fe}(\text{NO}_3)_3 \cdot 9\text{H}_2\text{O}$, 98.5%), nickel nitrate hexahydrate ($\text{Ni}(\text{NO}_3)_2 \cdot 6\text{H}_2\text{O}$, 98.0%), copper nitrate trihydrate ($\text{Cu}(\text{NO}_3)_2 \cdot 3\text{H}_2\text{O}$, 99.0%), methanol (99.5%), ethanol (99.5%), potassium nitrate (KNO_3 , 99.0%), potassium nitrite (KNO_2 , 97.0%), potassium hydroxide (KOH, 85%), ammonium sulfate ($(\text{NH}_4)_2\text{SO}_4$, 99.0%), sodium hydroxide (NaOH, $\geq 96.0\%$), salicylic acid ($\text{C}_7\text{H}_6\text{O}_3$), sodium hypochlorite solution (NaClO, available chlorine 5.2% of aqueous solution), trisodium citrate dihydrate ($\text{C}_6\text{H}_5\text{Na}_3\text{O}_7 \cdot 2\text{H}_2\text{O}$), sodium nitroferrocyanide dihydrate ($\text{C}_5\text{FeN}_6\text{Na}_2\text{O} \cdot 2\text{H}_2\text{O}$), hydrochloric acid (HCl, 12 mol L^{-1}), sulfamic acid (99.5%), p-aminobenzenesulfonamide (98.0%), N-(1-Naphthyl) ethylenediamine dihydrochloride (98.0%), phosphoric acid (H_3PO_4 , $\geq 85.0\%$), and 1-propanesulfonic acid 3-(trimethylsilyl) sodium salt (DSS) were purchased from Sinopharm Chemical Reagent Co. Ltd. Glyoxylic acid solution ($\text{C}_2\text{H}_2\text{O}_3$, 50 wt%), dimethyl sulfoxide- d_6 (DMSO- d_6 , 99.9 atom% D), ($^{15}\text{NH}_4$) $_2\text{SO}_4$ (99.0 atom% ^{15}N), and K^{15}NO_3 (99.0 atom% ^{15}N) were purchased from Aladdin Chemistry Co., Ltd (Shanghai, China). Bipolar membrane (TRJBM) were purchased from Beijing Tingrun Membrane Technology Development Co., Ltd (Beijing, China). The deionized (DI) water was produced using a Millipore Milli-Q grade, with a resistivity of 18.2 M Ω cm. All of the chemicals were used without any further purification.

Instrumentations

TEM images were taken using a Hitachi HT7700 transmission electron microscope at an acceleration voltage of 100 kV. HAADF-STEM and the corresponding EDS elemental mapping were carried out on a Talos F200X field-emission transmission electron microscope operated at an accelerating voltage of 200 kV using Mo-based TEM grids. Aberration-corrected HAADF-STEM images were carried out on Themis Z field-emission transmission electron microscope operating at an accelerating voltage of 300 kV using Mo-based TEM grids. XRD patterns were collected using a Rigaku MiniFlex X-ray diffractometer with $\text{Cu-K}\alpha$ radiation ($\lambda = 1.54059 \text{ \AA}$). ICP-OES (Avio 220 MAX, PerkinElmer) analysis was employed to measure the concentration of metal species. XPS measurements were performed using a Kratos Axis supra+ diffractometer with Al-K α radiation. The Raman spectra were conducted via LabRAM HR Evolution (Horiba) Raman system with a 532 nm excitation laser. The absorbance data was measured on a UV-vis spectrophotometer (Agilent Technologies, Cary 60). The in situ FTIR spectra were acquired by a Nicolet iS50 FTIR spectrometer with a built-in MCT detector.

Synthesis of $\text{Cu}_1\text{-N-C}$

A mixture of $\text{Zn}(\text{NO}_3)_2 \cdot 6\text{H}_2\text{O}$ (5.6 mmol) and $\text{Cu}(\text{COOCH}_3)_2 \cdot \text{H}_2\text{O}$ (0.28 mmol) was dissolved in 80 mL of methanol, which was subsequently added into 80 mL of methanol containing 3.70 g of 2-MeIm. Then the mixed solution was kept at 25 °C for 12 h. The as-obtained precipitate (denoted as Cu-doped ZIF-8) was separated by centrifugation and washed subsequently with methanol for five times, and finally dried at 65 °C under vacuum overnight. Next, the obtained Cu-containing derivative of ZIF-8 was heated to 900 °C with a heating rate of 5 °C min^{-1} in a tube furnace and kept at 900 °C under flowing Ar gas for 3 h. After the tube furnace was naturally cooled to room temperature, $\text{Cu}_1\text{-N-C}$ was obtained and directly used as the catalyst without further treatment. For comparison, Co single atoms anchored on N-doped carbon (denoted as $\text{Co}_1\text{-N-C}$) and Co single atoms

anchored on $\text{Cu}_1\text{-N-C}$ (denoted as $\text{Co}_1\text{Cu}_1\text{-N-C}$) were obtained via pyrolyzing the Co-doped ZIF-8 and Cu/Co-doped ZIF-8, respectively. Co-doped ZIF-8 and Cu/Co-doped ZIF-8 prepared with the similar procedure with that of $\text{Cu}_1\text{-N-C}$ except the $\text{Co}(\text{NO}_3)_2 \cdot 6\text{H}_2\text{O}$ and the mixture of $\text{Co}(\text{NO}_3)_2 \cdot 6\text{H}_2\text{O}$ and $\text{Cu}(\text{COOCH}_3)_2 \cdot \text{H}_2\text{O}$ as the metal precursors, respectively.

Synthesis of $\text{Co}_3\text{O}_4/\text{Cu}_1\text{-N-C}$ and $\text{Co}_3\text{O}_4/\text{N-C}$

160 mg of $\text{Cu}_1\text{-N-C}$ was dispersed in 20 mL of ethanol by sonication for 30 min. Afterwards, 5 mL of H_2O containing 45 mg of $\text{Co}(\text{NO}_3)_2 \cdot 6\text{H}_2\text{O}$ was added into the above solution, which was maintained in an ice-water bath for 1 h with vigorous stirring. Then, 40 mL of freshly prepared NaBH_4 (100 mg) with ice-cold H_2O was added dropwise into the above suspension, followed by further stirring for 1 h. The as-obtained precipitate was separated by filtration and washed subsequently with water for five times. Finally, $\text{Co}_3\text{O}_4/\text{Cu}_1\text{-N-C}$ was obtained by being dried at 65 °C under vacuum overnight. $\text{Co}_3\text{O}_4/\text{N-C}$ was prepared as a comparison with the similar procedure with that of $\text{Co}_3\text{O}_4/\text{Cu}_1\text{-N-C}$ except for the addition of N-doped carbon instead of $\text{Cu}_1\text{-N-C}$. N-doped carbon was prepared with a similar synthetic procedure with that of $\text{Cu}_1\text{-N-C}$ without the addition of $\text{Cu}(\text{COOCH}_3)_2 \cdot \text{H}_2\text{O}$. For comparison, other metal oxides including FeO_x , CuO_x , and NiO_x dispersed on N-doped carbon (denoted as $\text{FeO}_x/\text{N-C}$, $\text{CuO}_x/\text{N-C}$, and $\text{NiO}_x/\text{N-C}$, respectively) were prepared with the similar procedure with that of $\text{Co}_3\text{O}_4/\text{N-C}$ except for the addition of $\text{Fe}(\text{NO}_3)_3 \cdot 9\text{H}_2\text{O}$, $\text{Cu}(\text{NO}_3)_2 \cdot 3\text{H}_2\text{O}$, and $\text{Ni}(\text{NO}_3)_2 \cdot 6\text{H}_2\text{O}$ as the metal precursors, respectively (denoted as $\text{FeO}_x/\text{N-C}$, $\text{CuO}_x/\text{N-C}$, and $\text{NiO}_x/\text{N-C}$, respectively).

X-ray absorption fine structure (XAFS) measurements

The XAFS spectra at Cu K -edge and Co K -edge were performed at 1W1B beamline of Beijing Synchrotron Radiation Facility and BL11B beamline of Shanghai Synchrotron Radiation Facility. The data were obtained in ambient conditions under fluorescence mode for Cu K -edge and transmission mode for Co K -edge, respectively.

The ATHENA module and ARTEMIS codes in the IFEFFIT software packages were employed to extract the data and fitted the profiles^{32–34}. The k^3 -weighted EXAFS spectra were acquired by energy calibration and spectral normalization. For the EXAFS part, the Fourier transformed data in R space of Cu K -edge and Co K -edge were analyzed by applying a hanning windows ($dk = 1.0 \text{ \AA}^{-1}$) to differentiate the EXAFS oscillation from different coordination shells. Subsequently, we performed the least-squares curve parameter fitting to attain the structural parameters around central atoms. The fitted ranges of k space were set at 3.4–13.2 \AA^{-1} with R range of 1.2–3.0 \AA . The four parameters including coordination number (CN), bond length (R), Debye-Waller factor (σ^2), and E_0 shift (ΔE_0) were fitted without anyone being fixed, constrained, or correlated.

The in situ Cu K -edge XAFS measurements were conducted were collected with a home-made XAFS cell. Typically, 8 mg of the catalysts and 40 μL of Nafion were dispersed in 2 mL of ethanol by sonication for 1 h. Then the uniform ink was loaded onto carbon paper with an area of $2 \times 2 \text{ cm}^2$. The mass loading was calculated to be 2 mg cm^{-2} . The prepared catalysts, a Ag/AgCl electrode, and a Pt wire were used as the working electrode, reference electrode, and counter electrode, respectively. All electrochemical tests were measured in 1M KOH electrolyte with 1M KNO_3 (45 mL) and controlled by a CHI1140C electrochemical workstation.

Preparation of the working electrodes

8 mg of the catalysts were dispersed in 2 mL of ethanol by sonication for 1 h. Then 40 μL of Nafion solution was added to the mixture and sonicated for 30 min to obtain a uniform ink. Finally, the uniform ink was loaded onto carbon paper with an area of $2 \times 4 \text{ cm}^2$. The mass loading was calculated to be 1 mg cm^{-2} . The area of working electrodes used in the electrochemical measurements was 0.25 cm^2 .

Electrochemical measurements

The electrochemical measurements were carried out in an H-cell system which was separated by a bipolar membrane with a CHI1140C electrochemical workstation (Chenhua, Shanghai). Ag/AgCl electrode and graphite rod were used as the reference electrode and counter electrode, respectively. For NO₃⁻ electroreduction, 1 M KOH containing 1 M KNO₃ solution (60 mL) was evenly distributed to the cathode and anode compartments. The pH value of the electrolyte was determined to be 14 by a FiveEasy Plus pH Meter (METTLER TOLEDO). The applied potentials were measured against the Ag/AgCl reference electrode with 50% *iR* compensation and converted to the RHE reference scale by $E(\text{vs RHE}) = E(\text{vs Ag/AgCl}) + 0.21 \text{ V} + 0.0591 \times \text{pH} - iR$. The solution resistance was determined to be $4.4 \pm 0.2 \text{ ohm}$ in the electrolytes by potentiostatic electrochemical impedance spectroscopy at frequencies ranging from 10 Hz to 100 kHz, which was conducted in a standard three-electrode system at ambient conditions. Before the electroreduction test, CV curves were performed until the polarization curves achieved steady-state ones with a scan rate of 10 mV s^{-1} . Before the electrolysis, Ar gas was delivered into the cathodic compartment at a rate of 10 mL min^{-1} to remove dissolved O₂. The LSVs of the catalysts were recorded at a scan rate of 5 mV s^{-1} in 1 M KOH containing 1 M KNO₃/KNO₂. The controlled potential electrolysis was performed at applied potentials for 10 min. NO₂⁻ electroreduction was conducted with the same conditions except that the solution of 1 M KOH containing 1 M KNO₂ was used as the electrolyte. An absorption cell containing 30 mL of 1 M HCl was set to effectively absorb the possible escaped NH₃ from the cathode cell. After the electrolysis at each applied potential, the concentration of NH₃ in the absorption cell was lower than $1 \mu\text{g mL}^{-1}$. In this case, the volatilization of NH₃ from the electrolytes could be negligible. Cyclic voltammetric measurements were conducted in a non-faradaic potential window with various scan rates from 50 to 100 mV s^{-1} . C_{dl} was calculated by plotting the Δj ($\Delta j = j_a - j_c$) at the middle of the corresponding potential window against scan rates. The j_a and j_c were the anodic and cathodic current densities, respectively. The slope was twice of C_{dl} .

The calculation method for FE

The FE for the product (NH₃ and NO₂⁻) was calculated at a given potential as follows:

$$FE = C \times V \times N \times F / (Q \times M) \quad (1)$$

C: the measured concentration of product (mg mL^{-1}),
V: the volume of the electrolyte (mL),
N: the number of electrons transferred for the product, which is 8 for NH₃ and 2 for NO₂⁻,
F: Faraday constant, $96,485 \text{ C mol}^{-1}$,
Q: total electric charge (C),
M: the relative molecular mass, which is 17 g mol^{-1} for NH₃ and 46 g mol^{-1} for NO₂⁻.

The calculation method for the yield rate of NH₃ product

The yield rate of NH₃ product was calculated at a given potential as follows:

$$\nu_{\text{NH}_3} = (C_{\text{NH}_3} \times V) / (S \times t) \times 60 \quad (2)$$

ν_{NH_3} : the yield rate ($\text{mg}_{\text{NH}_3} \text{ h}^{-1} \text{ cm}^{-2}$),
*C*_{NH₃}: the measured concentration of NH₃ (mg mL^{-1}),
V: the volume of the electrolyte (mL),
S: the area of the catalyst (cm^2),
t: the reduction reaction time (min).

Determination of ion concentration

Determination of NH₃ concentration with indophenol blue method³⁵. After the electroreduction process, a certain amount of electrolyte was taken out from the electrolytic cell and diluted to the detection range. Then, 2 mL of 1 M NaOH solution containing salicylic acid (5 wt%) and sodium citrate (5 wt%) were added into the aforementioned solution, followed by the addition of 1 mL of 0.05 M NaClO and 0.2 mL of C₅FeN₆Na₂O (1 wt%). After standing in darkness for 2 h, the absorption spectra were measured using a UV-vis spectrophotometer. The concentration of indophenol blue was determined using absorbance at the wavelength of 650 nm. The concentration-absorbance curve was calibrated using standard (NH₄)₂SO₄ solution with a series of concentrations.

Determination of NH₃ concentration with ¹H NMR method. After NO₃⁻ electroreduction, a certain amount of electrolyte was taken out for further quantification by ¹H NMR (Bruker AVANCE AV III 400). All analyses were performed with 128-time scans. The concentration-integral area curve was calibrated using a standard (NH₄)₂SO₄ solution. Typically, (NH₄)₂SO₄ was dissolved in 20 mL of 1 M KOH electrolyte as a series of standard (NH₄)₂SO₄ solutions with different concentrations. Subsequently, 0.1 mL of dimethyl sulfoxide-*d*₆ (DMSO-*d*₆), 0.1 mL of 6 mM 1-propanesulfonic acid 3-(trimethylsilyl) sodium salt (DSS) solution, and 0.08 mL of 6 M HCl to adjust the pH value were added into 0.32 mL of (NH₄)₂SO₄ standard solutions with different concentrations. The signal appeared at 7.23, 7.10, and 6.97 ppm were attributed to NH₄⁺. The integral areas of the signal of NH₄⁺ were used to determine the concentration of (NH₄)₂SO₄ compared with the as-known DSS reference.

Determination of NO₃⁻ concentration³⁶. A certain amount of electrolyte was diluted to the detection range of NO₃⁻. Then, 0.1 mL of 1 M HCl and 0.01 mL of 0.8 wt% sulfamic acid solution were mixed with the diluted electrolyte, followed by shaking for 10 min. Using a UV-vis spectrophotometer, the absorption spectra were collected, obtaining the absorption intensities at a wavelength of 220 and 275 nm. Finally, the calculated absorbance ($A = A_{220\text{nm}} - 2A_{275\text{nm}}$) was acquired. The concentration-absorbance curve was calibrated using standard KNO₃ solutions with a series of concentrations.

Determination of NO₂⁻ concentration. 4 g of *p*-aminobenzene-sulfonamide, 0.2 g of *N*-(1-Naphthyl) ethylenediamine dihydrochloride, and 10 mL of phosphoric acid were mixed with 50 mL of water as the color reagent. A certain amount of electrolyte was taken out from the electrolytic cell and diluted to the detection range. 1 mL of H₃PO₄ (5 M) was added to the 4 mL of diluted post-electrolysis electrolytes to adjust the pH, followed by the addition of 0.1 mL of color reagent. After standing for 20 min, the absorption spectra were measured using a UV-vis spectrophotometer. The absorption intensity at a wavelength of 540 nm was recorded. The concentration-absorbance curve was calibrated using standard KNO₂ solution with a series of concentrations.

Determination of other liquid and gaseous product

The amount of NH₂OH was determined by ¹H NMR after NH₂OH was captured by excess amount of C₂H₂O₃ through oximation process. Specifically, 0.4 mL of the electrolyte after the NO₃⁻ electroreduction was mixed with 10 μL of 50% C₂H₂O₃ solution, followed by the addition of 0.1 mL of DMSO-*d*₆ (99%) and 0.1 mL of 6 mM DSS solution. The integral area of the signal appeared at 7.46 ppm were used to determine the concentration of NH₂OH compared with the as-known DSS reference. In this work, the amount of NH₂OH was below the detection limit for both NO₃⁻ and NO₂⁻ reduction over Co₃O₄/Cu₁-N-C.

Nitrogen oxides including NO, NO₂, and N₂O have been detected by an infrared gas analyzer (THA100S). H₂ and N₂ have been detected by an on-line gas chromatograph (GC-2014) equipped with a flame ionization detector and a thermal conductivity detector.

The FE for gaseous products were calculated by the following equation:

$$FE = x \times V_{\text{gas}} \times N \times F / (Q \times V_m) \quad (3)$$

x : the measured mole fraction of product,
 V_{gas} : the total volume of the gas (L),
 N : the number of electrons transferred for the product, which is 3 for NO, 8 for N₂O, 2 for H₂ and 10 for N₂,
 F : Faraday constant, 96485 C mol⁻¹,
 Q : total electric charge (C),
 V_m : the molar volume of the gas, 24.5 L mol⁻¹.

Isotope labeling experiments

The isotopic labeling experiment used K¹⁵NO₃ with ¹⁵N enrichment of 99% as the feeding N-source to clarify the source of ammonia. 1 M KOH was used as the electrolyte and K¹⁵NO₃ with a concentration of 1 M was added into the cathode compartment as the reactant. After the electrolysis, 0.1 mL of DMSO-*d*₆ and 0.1 mL of 6 mM DSS solution were added into 0.4 mL of the electrolyte, followed by adding 0.05 mL of HCl (0.1 M) to adjust the pH of the solutions. Then the obtained ¹⁵NH₄⁺ was identified on a Varian 400 MHz NMR spectrometer (Bruker AVANCE AV III 400).

Kinetic evaluation

The electrolysis at -1.0 V *vs* RHE were conducted for different time to acquire the rate constant in 1 M KOH containing 1 M NO₃⁻ or 1 M NO₂⁻. The reaction constant (k_1 for NO₃⁻ reduction and k_2 for NO₂⁻ reduction) was calculated by plotting the concentration of NO₃⁻ or NO₂⁻ against the time of reaction, supposing that the concentrations of NO₃⁻ or NO₂⁻ declined exponentially as per first-order rate.

$$C_t = C_0 \exp(-k \times t) \quad (4)$$

C_0 : initial concentration of NO₃⁻ or NO₂⁻ (g mL⁻¹),
 C_t : the concentration of NO₃⁻ or NO₂⁻ at time t (g mL⁻¹),
 t : the time of reaction (min).

Adsorption experiments

To determine the adsorption capacities of Co₃O₄/Cu₁-N-C, Cu₁-N-C, and Co₃O₄/N-C, 5 mg of catalysts were added to each 25 mL of NO₃⁻ or NO₂⁻ solutions with the initial concentration of 1 M under stirring for 2 h, respectively. The solutions were separated by filtration using the 0.22 μm microporous membrane filter. For high concentration of NO₃⁻ or NO₂⁻, the solution was diluted before absorbance measurements. The adsorption capacity was calculated using the following equation:

$$q_e = (C_0 - C_e) \times V / m \quad (5)$$

q_e : the adsorption capacity (g g_{cat}⁻¹),
 C_0 : the initial concentration of NO₃⁻ or NO₂⁻ (g mL⁻¹),
 C_e : the measured concentration of NO₃⁻ or NO₂⁻ after the adsorption (g mL⁻¹),
 V : the volume of the electrolyte (mL),
 m : the mass of the catalyst (g).

In situ FTIR measurements

Using a Nicolet iS50 FTIR spectrometer (Thermo Scientific) with a built-in MCT detector, we obtained the in situ electrochemical FTIR spectra. Typically, 2 mg of catalysts and 20 μL of Nafion dispersed in 2 mL of ethanol were sonicated for 1 h. Then the mixture was loaded onto the Au-coated Si prism to completely cover the Au film. The prepared prism was used as the working electrode after being dried naturally. The reference electrode and counter electrode was a Ag/

AgCl electrode and a Pt wire, respectively. The photograph of the in situ FTIR electrochemical cell was shown in Supplementary Fig. 36. All electrochemical tests were measured in 1 M KOH electrolyte with 0.1 M KNO₃ (30 mL) and controlled by a CHI1140C electrochemical workstation. All experiments were conducted at room temperature. The background spectra of the working electrode were obtained at an open-circuit potential before the electrochemical tests. All of the spectra were collected in absorbance by averaging 32 scans at a resolution of 4 cm⁻¹.

In situ Raman measurements

In situ Raman was carried out using Lab RAM HR Evolution (Horiba) equipped with a 50× microscope objective. The excitation wavelength was 532 nm with 10% intensity. The photograph of electrochemical cell for in situ Raman measurement was shown in Supplementary Fig. 37. Typically, 2 mg of catalysts and 20 μL of Nafion were dispersed in 2 mL of ethanol by sonication for 1 h. Then the electrocatalysts were deposited on fluorine tin oxide-coated glass as the working electrode. A Ag/AgCl electrode, and a Pt wire were used as the reference electrode, and counter electrode, respectively. All electrochemical tests were measured in 1 M KOH electrolyte with 1 M KNO₃/KNO₂ (5 mL) and controlled by a CHI1140C electrochemical workstation. All experiments were conducted at room temperature. Each spectrum was collected by integration twice, 60 s per integration. To determine the local concentration of NO₂⁻ near the surface of catalysts, we employed an internal standard method during the in situ Raman measurements.

DFT calculations

DFT calculations were performed using the Vienna Ab-Initio Simulation Package (VASP) code at the GGA level within the PAW-PBE formalism³⁷. DFT-D3 method with Becke-Jonson damping is performed for the van der Waals correction. The three-layer Co₃O₄ (100) slab model was adopted with a vacuum of 15 Å. The total energy calculations were performed using a 2 × 2 × 1 grid and a plane wave cut-off energy of 400 eV. Atoms in the bottom two layers were fixed. A U value of 3.5 eV was applied to the 3d states of Co to describe the strong on-site Coulomb interactions due to the localization of the Co 3d states³⁸. For the model of CuN₄ (no atoms were fixed), the total energy calculations were performed using a 3 × 3 × 1 grid and a plane wave cut-off energy of 400 eV. All atoms, which were not fixed, including adsorbates were allowed to relax until the force on each ion was smaller than 0.02 eV/Å.

We calculated the Gibbs free energy (G) for each species as follows:

$$G = E_{\text{DFT}} + E_{\text{ZPE}} - TS \quad (6)$$

where E_{DFT} , E_{ZPE} , and TS represent the DFT-optimized total energy, zero point energy (ZPE), and entropy contribution, respectively (T is the temperature, 298.15 K). It is assumed that $S = 0$ for all the adsorbed species.

Data availability

The data that support the findings of this study are available from the corresponding author upon request. The source data underlying Figs. 1–4 and Supplementary Figs. 1–44 are provided as a Source Data file. Source data are provided with this paper.

References

- Rosca, V., Duca, M., de Groot, M. T. & Koper, M. T. M. Nitrogen cycle electrocatalysis. *Chem. Rev.* **109**, 2209–2244, (2009).
- van Langevelde, P. H., Katsounaros, I. & Koper, M. T. M. Electrocatalytic nitrate reduction for sustainable ammonia production. *Joule* **5**, 290–294 (2021).

3. Wang, Y., Wang, C., Li, M., Yu, Y. & Zhang, B. Nitrate electroreduction: Mechanism insight, in situ characterization, performance evaluation, and challenges. *Chem. Soc. Rev.* **50**, 6720–6733 (2021).
4. Duca, M. & Koper, M. T. M. Powering denitrification: The perspectives of electrocatalytic nitrate reduction. *Energy Environ. Sci.* **5**, 9726–9742 (2012).
5. Xu, H., Ma, Y., Chen, J., Zhang, W. X. & Yang, J. Electrocatalytic reduction of nitrate - a step towards a sustainable nitrogen cycle. *Chem. Soc. Rev.* **51**, 2710–2758 (2022).
6. Fan, K. et al. Active hydrogen boosts electrochemical nitrate reduction to ammonia. *Nat. Commun.* **13**, 7958 (2022).
7. Li, J. et al. Efficient ammonia electrosynthesis from nitrate on strained ruthenium nanoclusters. *J. Am. Chem. Soc.* **142**, 7036–7046 (2020).
8. Wang, Y. et al. Structurally disordered RuO₂ nanosheets with rich oxygen vacancies for enhanced nitrate electroreduction to ammonia. *Angew. Chem. Int. Ed.* **61**, e202202604 (2022).
9. Deng, X., Yang, Y., Wang, L., Fu, X. Z. & Luo, J. L. Metallic Co nanoarray catalyzes selective NH₃ production from electrochemical nitrate reduction at current densities exceeding 2 A cm⁻². *Adv. Sci.* **8**, 2004523 (2021).
10. Zhang, X. et al. Recent advances in non-noble metal electrocatalysts for nitrate reduction. *Chem. Eng. J.* **403**, 126269 (2021).
11. Wang, X. et al. Free-standing membrane incorporating single-atom catalysts for ultrafast electroreduction of low-concentration nitrate. *Proc. Natl Acad. Sci. USA* **120**, e2217703120 (2023).
12. Zhang, G. et al. Tandem electrocatalytic nitrate reduction to ammonia on Mbenes. *Angew. Chem. Int. Ed.* **62**, e202300054 (2023).
13. Fu, Y. F. et al. Enhancing electrochemical nitrate reduction to ammonia over Cu nanosheets via facet tandem catalysis. *Angew. Chem. Int. Ed.* **62**, e202303327 (2023).
14. Fang, J. Y. et al. Ampere-level current density ammonia electrochemical synthesis using CuCo nanosheets simulating nitrite reductase bifunctional nature. *Nat. Commun.* **13**, 7899 (2022).
15. Zhu, T. et al. Single-atom Cu catalysts for enhanced electrocatalytic nitrate reduction with significant alleviation of nitrite production. *Small* **16**, e2004526 (2020).
16. Yang, J. et al. Potential-driven restructuring of Cu single atoms to nanoparticles for boosting the electrochemical reduction of nitrate to ammonia. *J. Am. Chem. Soc.* **144**, 12062–12071 (2022).
17. Li, P. et al. Pulsed nitrate-to-ammonia electroreduction facilitated by tandem catalysis of nitrite intermediates. *J. Am. Chem. Soc.* **145**, 6471–6479 (2023).
18. Cheng, X. F. et al. Coordination symmetry breaking of single-atom catalysts for robust and efficient nitrate electroreduction to ammonia. *Adv. Mater.* **34**, 2205767 (2022).
19. He, W. et al. Splicing the active phases of copper/cobalt-based catalysts achieves high-rate tandem electroreduction of nitrate to ammonia. *Nat. Commun.* **13**, 1129 (2022).
20. Wang, W., Chen, J. & Tse, E. C. M. Synergy between Cu and Co in a layered double hydroxide enables close to 100% nitrate-to-ammonia selectivity. *J. Am. Chem. Soc.* **145**, 26678–26687 (2023).
21. Liu, Y. et al. A highly efficient metal-free electrocatalyst of f-doped porous carbon toward N₂ electroreduction. *Adv. Mater.* **32**, 1907690 (2020).
22. Li, R. et al. Insights into correlation among surface-structure-activity of cobalt-derived pre-catalyst for oxygen evolution reaction. *Adv. Sci.* **7**, 1902830 (2020).
23. Wang, J. et al. Electrocatalytic reduction of nitrate to ammonia on low-cost ultrathin CoO_x nanosheets. *ACS Catal.* **11**, 15135–15140 (2021).
24. Gao, Q. et al. Synthesis of core/shell nanocrystals with ordered intermetallic single-atom alloy layers for nitrate electroreduction to ammonia. *Nat. Synth.* **2**, 624–634 (2023).
25. Song, Z. et al. Efficient electroreduction of nitrate into ammonia at ultralow concentrations via an enrichment effect. *Adv. Mater.* **34**, 2204306 (2022).
26. Gao, W. et al. Alloying of Cu with Ru enabling the relay catalysis for reduction of nitrate to ammonia. *Adv. Mater.* **35**, e2202952 (2023).
27. Wang, Y. et al. Enhanced nitrate-to-ammonia activity on copper-nickel alloys via tuning of intermediate adsorption. *J. Am. Chem. Soc.* **142**, 5702–5708 (2020).
28. Liu, H. et al. Efficient electrochemical nitrate reduction to ammonia with copper-supported rhodium cluster and single-atom catalysts. *Angew. Chem. Int. Ed.* **61**, e202202556 (2022).
29. Chen, F. Y. et al. Efficient conversion of low-concentration nitrate sources into ammonia on a Ru-dispersed Cu nanowire electrocatalyst. *Nat. Nanotechnol.* **17**, 759–767 (2022).
30. Wang, Y. T., Zhou, W., Jia, R. R., Yu, Y. F. & Zhang, B. Unveiling the activity origin of a copper-based electrocatalyst for selective nitrate reduction to ammonia. *Angew. Chem. Int. Ed.* **59**, 5350–5354 (2020).
31. Hao, R. et al. Pollution to solution: A universal electrocatalyst for reduction of all NO_x-based species to NH₃. *Chem. Catal.* **2**, 622–638 (2022).
32. Newville, M. IFEFFIT: Interactive XAFS analysis and FEFF fitting. *J. Synchrotron Radiat.* **8**, 322–324 (2001).
33. Ravel, B. & Newville, M. ATHENA, ARTEMIS, HEPHAESTUS: Data analysis for X-ray absorption spectroscopy using IFEFFIT. *J. Synchrotron Radiat.* **12**, 537–541, (2005).
34. Meng, Q. et al. Sustainable production of benzene from lignin. *Nat. Commun.* **12**, 4534 (2021).
35. Song, Z. et al. Promoting N₂ electroreduction into NH₃ over porous carbon by introducing oxygen-containing groups. *Chem. Eng. J.* **434**, 134636 (2022).
36. Bai, Y. et al. FCF-LDH/BIVO₄ with synergistic effect of physical enrichment and chemical adsorption for efficient reduction of nitrate. *Green. Energy Environ.* <https://doi.org/10.1016/j.gee.2023.05.011>, (2023).
37. Kresse, G. & Furthmüller, J. Efficiency of ab-initio total energy calculations for metals and semiconductors using a plane-wave basis set. *Comp. Mater. Sci.* **6**, 15–50 (1996).
38. Zasada, F. et al. Periodic DFT and HR-STEM studies of surface structure and morphology of cobalt spinel nanocrystals. Retrieving 3d shapes from 2d images. *J. Phys. Chem. C.* **115**, 6423–6432 (2011).

Acknowledgements

This work was supported by the Strategic Priority Research Program of the Chinese Academy of Sciences (XDB0450401), National Key Research and Development Program of China (2021YFA1500500, 2019YFA0405600), NSFC (22209161, 22302184, 22322901, 22221003, 22250007, and 22361162655), National Science Fund for Distinguished Young Scholars (21925204), CAS project for young scientists in basic research (YSBR-022, YSBR-051), China Postdoctoral Program for Innovative Talents (BX20200324), Collaborative Innovation Program of Hefei Science Center, CAS (2022HSC-CIP004), International Partnership Program of Chinese Academy of Sciences (123GJHZ2022101GC), the Joint Fund of the Yulin University and the Dalian National Laboratory for Clean Energy (YLU-DNL Fund 2022012), Fundamental Research Funds for the Central Universities, the Anhui Natural Science Foundation for Young Scholars (2208085QB41), and the Fellowship of China Postdoctoral Science Foundation (2021M693058). J.Z. acknowledges support from the Tencent Foundation through the XPLORER PRIZE. This work was partially carried out at the Instruments Center for Physical

Science, University of Science and Technology of China. This work was also partially carried out at the USTC Center for Micro and Nanoscale Research and Fabrication.

Author contributions

Z.G. and J.Zeng. supervised this project. Y.L. performed most of the experiments and analyzed the experimental data. J.W. conducted the in situ Raman measurements. Z.Y. and J.Zhao carried out DFT calculations and analyzed the computational data. L.Z. conducted the XAFS measurements and analyzed the results. Z.S., Y.Z., J.C., and J.M. provided help in materials synthesis and characterizations. Y.L., J.W., Z.G., and J.Zeng. wrote the manuscript. All authors discussed the results and assisted during manuscript preparation.

Competing interests

The authors declare no competing interests.

Additional information

Supplementary information The online version contains supplementary material available at <https://doi.org/10.1038/s41467-024-48035-4>.

Correspondence and requests for materials should be addressed to Zhigang Geng or Jie Zeng.

Peer review information *Nature Communications* thanks Aiqin Wang, and the other, anonymous, reviewer(s) for their contribution to the peer review of this work. A peer review file is available.

Reprints and permissions information is available at <http://www.nature.com/reprints>

Publisher's note Springer Nature remains neutral with regard to jurisdictional claims in published maps and institutional affiliations.

Open Access This article is licensed under a Creative Commons Attribution 4.0 International License, which permits use, sharing, adaptation, distribution and reproduction in any medium or format, as long as you give appropriate credit to the original author(s) and the source, provide a link to the Creative Commons licence, and indicate if changes were made. The images or other third party material in this article are included in the article's Creative Commons licence, unless indicated otherwise in a credit line to the material. If material is not included in the article's Creative Commons licence and your intended use is not permitted by statutory regulation or exceeds the permitted use, you will need to obtain permission directly from the copyright holder. To view a copy of this licence, visit <http://creativecommons.org/licenses/by/4.0/>.

© The Author(s) 2024